

Refined experimental studies for improving the reduced-scale physical modeling of seismic subsurface measurement

Damien Pageot^{*†}, Donatienne Leparoux^{*}, Mathieu Le Feuvre^{*}, Olivier

Durand^{*} and Yann Capdeville[†]

^{*}*LUNAM-IFSTTAR,*

[†]*OSUNA*

^{*}*LPGN,*

(March 4, 2016)

version 1.0

Running head: *Geophysics*

ABSTRACT

The potential of experimental seismic modeling at reduced scale is explored since several years because it provides an intermediate step between numerical tests and geophysical campaigns on field sites. In this scope, among the experimental benches using laser interferometry for recording ultrasonic data, the MUSC laboratory is designed as a reliable tool, able to produce experimental seismic reduced scale data from setup involving multi-sources and multi-receivers positions. The recorded signals contain the complete field suitable for high-resolution imaging techniques like Full Waveform Inversion. However, experimental seismic modeling uses a point-source and generates 3-D seismic data whereas most of wave propagation and imaging algorithms make use of 2-D forward modeling for numerical cost reasons. Further, geometrical spreading corrections applied on 3-D data are limited when

geological structures become complex. This leads to inaccurate relative amplitudes between wavefronts which can have an important impact on the quality of the recovered model of parameters. High-resolution imaging methods like FWI are also sensitive to the source waveform and the initial synthetic source must be, as the initial model, close enough to the true one. During the inversion process, the source wavelet can be estimated, per shot or for the whole dataset, but is strongly dependent of the initial model for inversion, *i.e.*, the estimated source will absorb inaccuracy of the initial model and the of update models. It results in ill-reconstruction of geological structures and parameter values. In this paper we seek to show the capacity of the experimental seismic modeling, like it is involved in the MUSC laboratory, to generate reproducible, realistic and suitable data which can be used as reference for 2-D high-resolution imaging method validations. In this scope, with the support of 2-D and 3-D numerical modeling algorithm based on the Spectral Element Method, we have first refined the comparison between numerical and experimental data by generating accurate experimental line-sources (2-D) which allow to avoid geometrical spreading correction of 3-D data. By this approach, we have shown the relevance of this step compared to corrections methods designed to 3D data and found in the literature, particularly when all the arrivals (surface waves and reflected body waves) need to be taken into account. Second, we have assessed the stability and the reproducibility of the source emitted in a model by the piezoelectric transducer during a campaign involving multi-sources multi-receivers acquisitions. The results of the source estimation through the 2D and 3D experimental setups as well as the reproducibility of the wave-shape contribute to refine the validation of the multi-source and multi-receiver measurement bench as an experimental seismic reduced scale modeling system and prove the capacity of ultrasonic devices used, associated to the positionnment bench to perfectly and quantitatively reproduce the seismic

surface measurements and the complete wave-field involved.

INTRODUCTION

Since the early developments of seismic imaging methods in the middle of 20th century, several approaches and algorithms innovations are still proposed in current research projects. The improvements deal with both the qualitative imaging techniques like migration (e.g. Berkhout et al. (2012); Guofeng et al. (2013)), novel applications of quantitative imaging
5 methods such as the first arrival tomography (e.g. Bohm et al. (2015)), or even more recent approaches like the Full Waveform Inversion (e.g. Perez Solano et al. (2014), see Virieux and Operto (2009) for a revue of this last decade). The refinements are proposed for different scales like near surface applications for civil engineering topics or more deeper investigation for example for oil prospection or crustal imaging at regional or global scales.
10 They are mostly validated by using synthetic data, for example with well known shared benchmark like the Marmousi model (Martin et al., 2006). However, the synthetic data are generally computed using the same wave propagation modeling engine used in the inverse problem process. This approach, called *inverse crime* (Wirgin, 2004) is particularly useful for validating an algorithm in its early development stage but does not take into account the
15 artifacts that can be due to the assumptions of the forward problem. Moreover, because no one knows precisely the Earth interior, it is difficult to evaluate the capacity of a method to recover physical parameters and structures from real seismic data which can lead sometimes to geological misinterpretation due to numerical artifacts (Morozov, 2004). Thus, it is necessary to add a step for which imaging methods will be tested for experimental seismic
20 measurements obtained under controlled conditions.

The best way to satisfy this need is to use Physical Small Scale Modeling Methods (noted *PSM* subsequently). *PSM* were used since several decades to study the propagation of

waves in various media with several stages of complexity, from acoustic wave propagation in homogeneous media to elastic wave propagation in 3-D heterogeneous anisotropic media.

25 The objectives of the approaches have firstly been addressed to understand the propagating waves phenomenology (for example Rieber, Howes) and in a second period for testing imaging process (Hiltermann, French, Bishop, Pratt, Isaac), or for validating numerical tools (Favretto-Cristini et al., 2013). For these different works, the technology used has become more and more sophisticated. Nowadays most of these benches involve piezoelectric

30 transducers to simulate multi-sources and multi-receivers (Wong et al., 2009) or immersed zero-offsets profiles (Favretto-Cristini et al., 2013). An other technique recently used is based on laser interferometry for recording the seismic signal without coupling effects in solid media (Bodet, Van Wijk, Breteau 2011,2013), or in gelee (). All these works have shown the relevance of carrying out experimental seismic data under well-controlled

35 conditions. However key points remain crucial if we seek to quantitatively simulate the complete seismic wave field recorded in case of seismic surface measurement generated with a hammer fall source, firstly because of the presence of surface waves that avoids the possibility of using immersed media and secondly because the emitted source pattern has to be omni-directional which implies a physical source point. In this aim, the MUSC (Mesures

40 Ultrasonores Sans Contact in french) system has been designed (Breteau et al., 2011) to simulate (1) wide-angle on-shore acquisitions modeling both body waves and surface waves, (2) automatic multisource-multireceiver measurements with a high-productivity, (3) high-precision source-receiver positioning and (4) high-precision recording of absolute surface displacement without coupling effects.

45 These abilities have been validated through a comparison of experimental data to numerical simulation in a 2D space containing a cavity (Breteau et al., 2011). The results showed

very fine similarities concerning the diffracted and converted arrivals when the source wave-
form is taken into account. For that, the numerical source was simulated in 2D and some
corrections were required to compare the amplitude results, with some remaining weak dis-
crepancies as mentioned in the discussion of Bretaudeau et al. (2011). The source diagram
was assessed with a parallel measurement bench, showing an omni-directional propagation.
However, 3D elastic wave propagation modeling methods are computationally expansives
and imaging methods are used mainly for 2D structures. Therefore, forward problems
implicitly use line-source in 3D-space while field and experimental data are acquired using
punctual sources which produce 3D wavefields.

This differences between 2D and 3D propagated wavefields must be take into account to
successfully validate imaging methods using field or experimental data.

Widely used methods consist in perform spreading transformations of 3D-wavefield for 2D-
media as a pre-processing step. Severl 3D-to-2D transformation techniques exist, all under
the assumption of a 1D media or a 2D media invariant along the axis perpendicular to the
strike direction.

Recently, Forbriger et al. (2014) have proposed the *hybrid* method which makes it possible
to correct geometrical spreading with a good accuracy for both near- and far-field data.
This method, described in a following section, is used in this study, essentially to compare
experimental and numerical data.

Another critical point for a successfull application of high-resolution imaging methods is the
knowledge of the source time function, generally treated as an unknown in the case of field
data. A known or, at least, a good approximation of the source excitation allows to avoid
source wavelet estimation during the inversion process and to facilitate the validation of

70 the imaging method. This source time function is quite easy to estimate from experimental data which support even more PSM as a validation tool for seismic exploration methods.

Our objective here is to complete the validation of the capability of ultrasonic devices to precisely and quantitatively simulate surface seismic data carried out with multi-sources and multi-receivers setting. This quantitative refined approach will increase the potential
75 of the MUSC laboratory as a reliable tool for generating experimental data which will be distributed in the scientific community and used as references for validation of seismic imaging methods. In this way, we further present two studies of experimental data in order to :

- 1) refine the quantitative comparison between numerical and experimental data by taking into account the 3D/2D geometrical spreading effects through an alternative way that we
- 80 compare to the corrections proposed in the literature ; 2) identify the reproducibility of the source impact and, consequently, data repeatability, and estimate source time functions usable for 2D imaging methods. These approaches will complete the knowledge of the system and facilitate the achievement of massive multi-source and multi-receiver data simulating subsurface seismic experimental campaigns. Moreover, they provide quantitative informa-
- 85 tions about the data quality for geophysicists who need to use them measurement based on reduced scale models.

In order to achieve these objectives, we used a seismic wave modeling code based on the Spectral Element Method (Komatitsch et al., 1998; Komatitsch and Tromp, 1999; Komatitsch et al., 2005; Festa and Vilotte, 2005) to provide numerical signals as reference
90 data for comparison.

The numerical characteristics of the code used are described in a first part below. Afterwards, the specificities of the MUSC laboratory are explained, followed by the presentation

of the models used. Finally The two coupled studies on experimental data are detailed, in the respective aims (1) of refining the comparison between numerical and experimental data by taking into account the geometrical spreading effects between 2-D and 3-D data through an alternative way, and (2) of identifying the reproducibility of the source impact to validate the data reproducibility.

METHODS

Numerical modeling: Spectral Element Method

For this study, we need a numerical modeling method which has a spatial discretization convenient for the representation of complex environments and provides high precision results as well as low numerical dispersion. Thus, we use the Spectral Element Method (SEM) for two-dimensional and three-dimensional elastic wave propagation modeling (Komatitsch et al., 1998; Komatitsch and Tromp, 1999; Komatitsch et al., 2005; Festa and Vilotte, 2005).

The SEM is a variant of Finite Element Method (FEM) (Lysmer and Drake, 1972; Seron et al., 1990; Hulbert and Hughes, 1990; Tromp et al., 2008) based on a high-order piecewise polynomial approximation of the weak formulation of the wave equation which leads to a spectral convergence ratio as the interpolation order increases. Considering near-surface experiments, one advantage of SEM is that the weak formulation naturally satisfy the free-surface condition which allows to simulate surface wave propagation with a great accuracy (Komatitsch and Vilotte, 1998; Komatitsch et al., 1999, 2005). Contrary to FEM, which have a variety of available element geometry (Dhatt and Touzot, 1984), SEM is limited to quadrilateral elements in 2D and hexaedral elements in 3D. Note that SEM on tetrahedral elements exists (Komatitsch et al., 2001) but leads to theoretical complications. However,

quadrangle and hexaedra are well suited to handle complex geometries and interface match-
115 ing conditions (Cristini and Komatitsch, 2012).

In SEM, the wave-field is expressed in terms of high-degree Lagrange interpolants and the integrals calculation are based on the quadrature of Gauss-Lobatto-Legendre (GLL). Each element is discretized with Lagrange polynomials of degree n_l and contains $n_l + 1$ GLL points which constitute their local mesh. This combination of high-degree Lagrange
120 interpolants with the GLL quadratic integration leads to a perfectly diagonal mass matrix which provides in turn a fully explicit time scheme suitable for numerical simulations on parallel computers (Komatitsch and Vilotte, 1998; Komatitsch et al., 1999).

The spatial resolution of SEM is controlled by the typical size of an element (Δh) and the polynomial degree in use on an element (n_l). Typically, a polynomial degree $n_l = 4$
125 are optimal for seismic wave propagation modeling (Moczo et al., 2011) even if $n_l = 8$ stay numerically affordable in 2D. For accurate results, required Δh is of the order of $\lambda_{min}/2 < \Delta h < \lambda_{min}$ for $n_l = 4$ and $\lambda_{min} < \Delta h < 2\lambda_{min}$ for $n_l = 8$, λ_{min} being the smallest wavelength of waves propagated in the model. The time marching scheme is governed by the stability CFL condition:

$$\Delta t < \mathcal{C} \frac{\Delta h}{c_{max}} \quad (1)$$

130 where \mathcal{C} is the Courant constant and c_{max} is the maximum wave velocity, typically the P-wave velocity. The Courant constant \mathcal{C} is determined empirically, depending on the application, and is fixed to a maximum of 0.30 for this study.

In our study, the models are meshed with quadrangles (2D) and hexaedras (3D) using the open-source software package GMSH (Geuzaine and Remacle, 2009).

135 **Physical modeling: MUSC laboratory**

The MUSC laboratory (Bretaudeau et al., 2008, 2011, 2013) is built to experimentally reproduce low noise field seismic data on reduced scale model. Figure 1 shows the measurement bench and its components : it is composed of a honeycomb tab and two arms which control the source and the receiver positions with a precision of $10\ \mu\text{m}$.

140 The receiving system of MUSC laboratory is a laser interferometer based on the phase shift of the reflected laser signal due to the particular displacement at the surface of the model during the seismic waves propagation in the medium. The diameter of the laser beam on the model surface equals 20 micrometers for the focal distance of 40 mm and makes it possible a detection of a vertical displacement of the order of the nanometer in the frequency range
145 from 10 kHz to 20 MHz. The laser interferometer constitutes a non-coupled receiver which avoids the complicated modeling of the coupling effects on measurement.

The seismic source in the MUSC laboratory is simulated by a piezoelectric transducer linked to a launching and synchronization system. It allows to choose the source function, i.e., a waveform like a Gauss or Ricker function, for a central frequency f_0 and a time delay
150 t_0 . For that, the source is generated by a waveform generator and is then amplified before being transmitted to the small-scale-model.

Since the wave equation is linear, the change of scale must keep the relationship between observables, i.e. amplitudes and time arrivals. About the amplitude, the quality factor Q is chosen to be in the same range as the materials of near surface. For the time scaling,
155 the key parameter is the ratio between the propagated seismic wavelength and the spatial dimensions of the experience which includes the model geometry, the spatial increment between the sources and the receivers positions, but also the dimensions of the source

impact. In the framework of seismic physical modeling, the latter must be as close as possible to a point source in order to simulate the spatial energy radiation pattern of a weight drop on the surface, i.e. with an omnidirectional emitted P-wave.

In the MUSC laboratory, the main frequency bands used for reduced scale data are [20 kHz ; 200 kHz] and [300 kHz; 800 kHz], respectively called here "low frequency band" and "high frequency band". For the lower spectral band, a commercial piezoelectric transducer is used without any coupling gel. For the higher band, the piezoelectric source is coupled through a conical adapter which is stuck to the transducer in order to obtain the expected impact surface. The resulting radiation patterns of the sources are constantly nearly omnidirectional for the range of recorded frequencies (see Bretaudeau et al. (2011) for details).

The lower frequency band is well adapted to simulate seismic experiment applied to near surface through the scales ratios proposed in tables 1 and 2. In the first case (table 1), a central frequency of 100 kHz in the laboratory corresponds to a central frequency of 100 Hz on the field, whereas in the second one (table 2) a central frequency of 100 kHz in the laboratory corresponds to a central frequency of 50 HZ on the field. Note that with these propositions, the quality factor Q and the density ρ are modeled with a ratio equal to 1, i.e. they remain the same at both of the scales. Actually small-scale models are generally made of thermoplastic or casting epoxy resin materials (Bretaudeau et al., 2013). The mechanical properties of these materials provide attenuation characteristics close to natural soil materials of subsurface media. Their seismic velocities are about 2 times of those in subsurface materials as proposed in table 2. The possibilities of combinations can generate the impedance contrasts encountered in the geophysical issues.

The MUSC bench presented above has been studied for simulating with a great repro-

ducibility the typical field campaigns of subsurface seismic measurement. The validation was achieved by comparison between small scale measurement and numerical data (Bretaudeau et al., 2011). Results have shown a great reproducibility of the converted and diffracted events recorded on the vertical component. The amplitudes analysis had been
185 conducted through 2D-3D corrections and small discrepancies remained due to the difficulty of taking into account the S and P waves in the same way. For this reason, we propose here to refine the study by testing a more recent correction methodology Schafer et al. (2014) as well as providing experimental and numerical, 2D and 3D data. This approach will be achieved through data carried out on two models that are presented below.

190 **Characteristics of the scale models tested**

In this study, we consider two different reduced scale models. The first one is homogeneous whereas the second one contains a deeper layer with a geometrical variation of the interface along the profile. The top layer, as well as the entire first model, is made of epoxy-resin called F50. The deeper layer is built with a more dense resin called LAB1000. Latter model
195 is named *BiAlt*. The specific properties of these two kinds of resins are summarized in the table 3. As required, note that the Q-factor values are of the same order of the Q-factor value in the shallowest parts of some natural media.

As described in the previous part and proposed in table 2, it is possible to take into account a scale ratio equal to 2 between real and reduced model velocities, makes it possible to
200 use a 100 kHz Ricker source in order to simulate a 50 Hz Ricker source in reality, which is realistic for simulating an hammer impact on the surface. In this case, the distance scale ratio is 1000 such that a 1 mm distance in the laboratory experiment corresponds to a 1 m

distance in reality.

In a next section, the recorded signals will be finely analyzed for a maximum offset equal
205 to 60 mm in the case of the homogeneous model and 100 mm for the *BiAlt* model. Thus,
the resin models have to be wide enough in order to carry out this receiver-source distances
without providing boundary echoes which could interfere with the direct arrivals. For that,
the homogeneous model is 500 mm long and 504 mm large and 115 mm high. The *BiAlt*
model is 540 mm long, 300 mm large and 203 mm high. The geometry is presented in figure
210 3 and simulates an interface between a 3 m thick layer of clay overcoming a limestone layer.

The numerical meshing required for numerical simulations involve dimensions of cells about
 $e_s < 3.43 \text{ mm}$ for F50 material and $e_s < 4.66 \text{ mm}$ for the LAB1000 material, considering
a polynomial degree $n_l + 1 = 5$ and a slightly over-estimated maximum frequency $f_{max} =$
300 *kHz* for $f_0 = 100 \text{ kHz}$. The resulting meshing structure for the *BiAlt* model is presented
215 figure 4.

These two resin blocks as well as their corresponding numerical models will be used for gen-
erating seismic data with punctual sources and line sources, for the homogeneous model,
in order to study the effective source excitation emitted in the MUSC bench and its repro-
ducibility.

220 3D/2D differences

Most of seismic imaging methods implement a 2D forward problem, essentially for numerical
cost reasons. It results in an implicit use of 2D line-source, invariant along the direction per-
pendicular to the strike direction, while field data are generally acquired using point-source
(hammer-blow, mass). Consequently, it exists differences in amplitude and phase between

225 point-source and line-source responses which must be considered in the case inversion of
field data with a 2D imaging method.

The displacement field u can be evaluated at general position and time (\mathbf{x}, t) by (Aki and
Richards, 2002):

$$u(\mathbf{x}, t) = \int_{-\infty}^{+\infty} d\tau \int \int \int_V G(\xi, t - \tau; \mathbf{x}, 0) f(\xi, \tau) dV(\xi) , \quad (2)$$

where $G(\xi, t - \tau; \mathbf{x}, 0)$ is the Green's function and $f(\xi, \tau)$ is the seismic source function.

230 The body force distribution for a point source f_P and a line source (f_L) for a 2D structure
 $G(\xi, t - \tau; \mathbf{x}, 0)$ invariant along y-axis at position $\mathbf{x}_s = (x_s, y_s, z_s)$ are:

$$f_P(\mathbf{x}, t; \mathbf{x}_s) = \mathbf{F}(t) \delta_{\mathbf{x}}(x - x_s) \delta_{\mathbf{x}}(y - y_s) \delta_{\mathbf{x}}(z - z_s) , \quad (3)$$

$$f_L(x, y, z, t; x_s, z_s) = \mathbf{F}(t) C \delta_{\mathbf{x}}(x - x_s) \delta_{\mathbf{x}}(z - z_s) , \quad (4)$$

Substituting equation 3 in equation 2 and equation 4 in equation 2 lead to the wave motion
due to a point-source u_P and the wave motion due to a line-source u_L

$$u_P(\mathbf{x}, t; \mathbf{x}_s) = \int_{-\infty}^{+\infty} G(\mathbf{x}_s, t - \tau; \mathbf{x}, 0) F(\tau) d\tau, \quad (5)$$

$$u_L(x, y, z, t; x_s, z_s) = \int_{-\infty}^{+\infty} \int_{-\infty}^{+\infty} G(x_s, y', z_s, t - \tau; \mathbf{x}, 0) F(\tau) C dy' d\tau , \quad (6)$$

The equivalent displacement u_L for a line-source can be obtain from the displacement field

235 u_P generated by a point source by integration along y :

$$u_L(x, y, z, t; x_s, z_s) = \int_{-\infty}^{+\infty} u_P(x, y, z, t - \tau; x_s, y', z_s, 0) C dy' . \quad (7)$$

Latter means that in term of amplitude, the displacement generated by a line-source is greater than displacement generate by a point-source.

Taking $g_k^{3D}(r)$ and $g_k^{2D}(r)$, the Fourier transform of the 3D and 2D Green's function in the acoustic approximation, respectively, with k the wavenumber and $r = |\mathbf{x} - \mathbf{x}_s|$ the
240 source-receiver offset. In the far-field approximation, Forbriger et al. (2014) demonstrate:

$$\lim_{r \rightarrow \infty} \frac{g_k^{2D}(r)}{g_k^{3D}(r)} \approx \sqrt{\frac{2\pi r}{k}} \cdot e^{i\frac{\pi}{4}} . \quad (8)$$

Replacing the wavenumber $k = \omega/v_{ph}$, where ω is the angular frequency and v_{ph} is the phase velocity, it results:

$$\sqrt{2\pi r v_{ph}} \cdot \sqrt{\frac{\pi}{\omega}} e^{i\frac{\pi}{4}} = F_{amp} \cdot \tilde{F}_{\sqrt{t-1}} , \quad (9)$$

where F_{amp} is the amplitude factor and $\tilde{F}_{\sqrt{t-1}}$ applies the phase shift. It results in:

$$u_L(r, \omega) = u_P(r, \omega) \cdot F_{amp} \cdot \tilde{F}_{\sqrt{t-1}} . \quad (10)$$

This correction is called the *single-velocity* transformation which is recommended for small
245 offset. For larger offset, stating that offset is almost equal to the propagation distance, Schafer et al. (2014) propose to replace the previous amplitude factor with:

$$F_{amp} = r \sqrt{\frac{2\pi}{t}} . \quad (11)$$

The resulting correction is called the *direct-wave* transformation. Finally, the *hybrid* transformation proposed by Forbriger et al. (2014) and Schafer et al. (2014) consists to use

both previous transformation with smoothly offset conditioned transition from near-field to
 250 far-field.

The *hybrid* method was successfully validated by Schafer et al. (2014) in terms of modeling and reconstruction tests with a 2D FWI method and 3D numerical data generated in a 2D structure. Given its performance, the *hybrid* is used in the next sections for comarisons with experimental data.

RESULTS

255 From point-source to line-source response

The approach detailed here consists in generating data with a 2D line-source as well as a 3D point-source and analyzing the similarity to numerical results under the same conditions. This is conducted to answer to two needs : 1) the quantitative refined validation of the reduced scale data , 2) the validation of the reduced scale data as a 2D set which is
 260 intermediate between numerical simulation and field data suitable for the 2D imagery tests . Indeed, in the framework of wave propagation modeling and imaging methods, even if 3-D acoustic algorithm exists (Ben-Hadj-Ali et al., 2008; Plessix et al., 2010) and 3-D elastic algorithm are always in development (Castellanos et al., 2011; Borisov and Singh, 2015), most of available algorithms are limited to the 2-D elastic and 3-D acoustic approxima-
 265 tion especially for computational cost causes. More, a widely used way to validate imaging methods consists in inverse crime while the validity of applications on real dataset is conditioned by strong *a priori* and a weak knowledge of the target. All of these leads to a limited validation of the efficiency of imaging methods to recover parameter models. Thus, it is critical for 2-D inversion of field data to accurately correct the difference between 2-D

270 and 3-D geometrical spreading.

The *hybrid* method, presented in the previous section, is an efficient spreading transform which makes it possible to reconstruct velocity models with 2D-FWI method using 3D-data. However, this method is derived from a far-field acoustic approximation of Green’s functions and is known to fail for back-scattered surface wave (Schafer et al., 2014). Moreover, 275 the correct smooth transition between *single-velocity* and *direct-wave* transformations is not easy to determine without 2D reference data. This is the case for both field and experimental data and the spreading transformation results become strongly dependant of the user’s attempts and experience.

Thus, the missing step between purely numerical validation and real data applications 280 can be addressed by an alternative approach that consists in recording experimental seismograms generated by line-sources under controlled conditions. Here, we take advantage of the experimental framework to explore this alternative approach specific through the MUSC laboratory, *i.e.* caring out 2D measurement from 2D source-lines. Figure 5 shows a schematic representation of the principle for this kind of experiment. The line-source is 285 composed of a finely-sampled line of point-source and a line of receiver for each considered offset.

Taking advantage of the reciprocity principle in case of a vertical source and a vertical component recording, the experiment can be simplified by considering only one receiver per offset, on a line perpendicular and centered to the defined line-source. All traces of each 290 common receiver gather are then stacked together to obtain the line-source response. In order to apply this protocol, we have to choose a suitable sampling interval Δs between each point-source constituting the pseudo line-source to ensure applicability of the *Huygens*

principle. Given the material properties of *F50 pure* epoxy-resin, we choose an interval $\Delta s = \lambda_{min}/10 \approx 0.5 \text{ mm}$ over a line of 300 mm long which leads to 601 point-source positions.

295 Four receiver positions are available: 45, 50, 55 and 60 mm offset. The source time function (for the numerical simulation as well as for the experimental test) is a Ricker, the second derivative of a Gaussian:

$$s(t) = (1 - 2(\pi f_0(t - t_0))^2) e^{-(\pi f_0(t - t_0))^2}, \quad (12)$$

where f_0 is the central frequency and t_0 is the peak time. Here, we take a central frequency $f_0 = 100 \text{ kHz}$ and $t_0 = 0.03 \text{ ms}$. The obtained data set are filtered using a low-pass
300 Butterworth filter with a cutoff frequency $\omega_c = 250 \text{ kHz}$ to remove noise and are tapered at the beginning using a cosine taper function of width $w = 0.03 \text{ ms}$ on the time signal. Figure 6 shows the results for both numerical simulation and experimental data. The signals emitted by a line of point-sources and recorded at the first receiver position (45 mm) are presented in figures 6(a,c) for the numerical and experimental tests respectively. Note there
305 is no attenuation accounted for the numerical modeling, so we do not compare directly numerical and experimental results. Moreover, all the resulting traces are normalized to be comparable to the experimental tests. The numerical result (fig 6(a)) clearly shows the direct attempted P and S wavefronts and the reflected PP and P-SV wavefronts as mentioned (labels 1, 2, 3, 4 on figure 6). These similarities between numerical simulation
310 and experimental data are altered by multiple echoes visible on experimental data (labeled E on figure 6(b)), as a ringing effect on the source wavelet due to the piezoelectric transducer coupling on the model surface. This point will be addressed in the next section focused on the source reproducibility.

The comparisons of the point-source and line-source responses are presented in figures 6(b) and 6(d), respectively for numerical and experimental modeling. Here, the point-source response (red line signals in the figures) corresponds to the central trace (distance 0 mm) visible on figures 6(a) and 6(c) and the equivalent line-source response (green line signals) is the weighted stack of all traces shown on the same figures (6(a,c)). An other reference is taken into account for numerical modeling, i.e. we provide a line-source response from 2-D modeling (blue line signal in figure 6(d)) for a comparison of both 3-D and weighted stack results. First, figure 6(b)) shows that the two numerical reference signals are not distinguishable : the blue and green lines signals are perfectly superimposed until 0.18 ms, afterward the the PSv wave amplitude (i.e. the latter arrival) is abnormally high in case of sampled source line. This effect can be related to the limited dimensions in time and space of the original 3-D setup. Nevertheless, the global adequation highlights the validity of sampling a source-line by a set of source points as we proposed, but subject to the boundary effects. Second, in each case (numerical and experimental ones), the comparison between 2D and 3D experiments show clearly the attempted phase shift of $\pi/4$ between the point-source and the line-source responses. Some differences in terms of waveform, clearly visible for the experimental results occur between 0.08 and 0.10 ms. We will focus on this particularity concerning the analysis of the corrected data in the following.

A similar comparison, for the four source-receiver offsets, are shown in figures 7(a) and 7(b) for numerical modeling and experimental modeling, respectively. Moreover, in order to test the improvement of our approach to provide an experimental source-line response in comparison to the recent correction developed to transform 3D toward 2D data, which is described above, we have applied and calibrated the *hybrid method* (Forbriger et al., 2014; Schafer et al., 2014) on the numerical source-point response and we thus obtained the

estimated equivalent line-source response. Figure 7(b) presents the comparison between
 the numerical line-source response and the equivalent line-source response and shows that
 340 the *hybrid method* is able to produce the equivalent line-source response with a very good
 agreement in terms of both phase and amplitude for direct P and S -waves. However, PP
 and PSv reflected waves remain weakly different. Finally, we have applied the correction
 with the same calibration to the experimental signal (figure 7(d)). This last result also
 shows a good agreement between experimental line-source responses and those obtained by
 345 the correction through the hybrid method up to 0.12 *ms*, i.e. for the direct waves. Note
 that the wave shape differences visible between 0.8 and 0.10 ms in 7(c), similar to those
 mentioned above are well corrected in 7(d). However, discrepancies occur for the reflected
 arrivals : the first reflected arrival (i.e. the P-P reflected wave) is marked by the red line
 on figures 7(b,d). These unagreement are greater than in the numerical case: the correction
 350 of the geometrical spreading through the hybrid method seems unable to scale correctly
 amplitude where echoes of the source and reflected wave are interfering. For this reason,
 an experimental 2D source-line should be recommended instead of the hybrid correction of
 data in order to take into account all the seismic arrivals in the data. Concerning the signal
 recorded at the 55 *mm* offset, the largest amplitude difference can be explained by a weaker
 355 *signal-to-noise* ratio than for the three other offsets in the experimental data.

These results about our approach to generate experimental line-source responses show that
 the MUSC laboratory is efficient and can produce reliable 2D experimental data suitable
 for migration-based methods such as FWI. Thus, it plays the role of an intermediate tool
 that provides 3D or 2D data without the necessity of phase and amplitude corrections.

360 Experimental source reproducibility

In the framework of high-resolution imaging, such as FWI, first validations of the method are generally performed on the basis of inverse crime or using synthetic data from an other modeling code. In these cases, the source waveform is known and the initial model m_0 is generally a smoothed version of a known *true model* used in the forward problem to obtain
 365 synthetic observed data. Consequently, no source wavelet estimation is done. However, the knowledge of the source waveform is an important task when real data are inverted. In many cases, efficient sources are recovered using a linear source wavelet estimation method (Pratt, 1999) which integrates the whole signal such as:

$$S_{est}(\omega) = \sum_{i=1}^{N_R} \frac{G_i(\omega)H_i(\omega)^*}{G_i(\omega)G_i(\omega)^*} S, \quad (13)$$

where ω is the angular frequency, S_{est} is the real Fourier transform of estimated source, $G(\omega)$
 370 is the real Fourier transform of the observed signal, $H(\omega)$ is the real Fourier transform of the signal calculated in the synthetic model, $S(\omega)$ is the synthetic source used to compute $H(\omega)$, N_R is the number of receivers and $*$ denotes the conjugate. The main issue of this method is that inaccuracies in the synthetic model, and consequently in the calculated data, are integrated in the estimated source. For example, () show that the intrinsic attenuation
 375 of the medium can affect the source wavelet inversion if the direct problem does not take into account the Q factor or if it is not well known. The resulting distortion of the estimated source wavelet can lead to inaccuracies in the updated models during the data inversion and then in the recovered parameters of the final model. Moreover, for a given dataset, one or more specific sources need to be estimated, depending if the source is considered stable
 380 enough from a shot to another or not. However, estimating the source for each shot in case

of numerous multi-sources/multi-receivers data can quickly provides a significant additional numerical cost. Thus, the knowledge of the source waveform and its stability are two crucial key points in modeling experimental data for testing the imaging processes.

We have shown in the previous section that the MUSC laboratory is able to generate high
 385 quality 2D experimental seismograms. Then, if the source waveform is constant during an experiment, it will be very efficient for imaging method validation. As shown by Bretaudeau et al. (2011), the source waveform injected in the reduced-scale model by the piezoelectric source is not similar to the selected theoretical one. Indeed, Figures 6(c) and 6(d), in previous section, show multiple wavefront following the first arrival one. These multiples
 390 echoes are due to the coupling of the piezoelectric source on the material before that the wavelet is injected in the model. It can depend on the material as well as the force applied on the transducer. So it naturally raises question about the ability of the MUSC laboratory to provide reproducible sources, during a complete multi-sources/multi-receivers experiment. Thus, in order to evaluate the reproducibility of the source impact, several numerical and
 395 physical modeling described below have been performed on the same *F50 pure* homogeneous epoxy-resin block as in previous section. s

In a first step, ten events have been acquired on this model with a similar geometry setup: 120 receivers positions with an increment $\Delta r = 1 \text{ mm}$ and a minimum source-receiver offset of $O = 10 \text{ mm}$ (see figure 8). The numerical wavelet sent to the piezoelectric transducer
 400 source is a Ricker function with a central frequency of 100 kHz and $t_0 = 0.03 \text{ ms}$. Each data set was filtered using a low-pass Butterworth filter with a cutoff frequency $\omega_c = 250 \text{ kHz}$ to remove noise and tapered at the beginning and end using a cosine taper function of width $w = 0.03 \text{ ms}$. Then, a 3D/2D geometrical spreading correction was applied using the *hybrid* method with a linear offset dependent ratio $r = O/O_{max}$, where O_{max} is the

405 maximum source receiver offset. As shown previously this correction is well adapted to
 correct the direct arrival which will be preferentially taken into account for determining
 the source wavelet. Figure 9(a) shows the resulting central trace ($o = 70 \text{ mm}$) of each
 realization (red line signals) compared to a reference central trace resulting from average
 of traces for the same offset (green line signal). The good agreement between the central
 410 traces and the reference signal is a first validation of the reproducibility of the source in
 a same experiment. This agreement is enforced by the correlation coefficient (cc) greater
 than 0.98 in each case. In a second step, to go further, a unique source wavelet is estimated
 using equation 13. As previously done, the signal used are normalized in order to avoid
 the intrinsic attenuation effects on the direct arrivals. The source wavelet estimation takes
 415 into account the vertical components of the ten experiments together and allows to obtain
 a mean effective source wavelet (figure 10). This effective source is very different of the
 theoretical one with a strong asymmetry around the main pulse at t_0 and a large sequence
 of source echo from $t = 0.04 \text{ ms}$ to the end of the time window. This source wavelet, applied
 to all synthetic signals should reproduce experimental data if the real source wavelet is the
 420 same for all experiments. The resulting traces are presented in figure 10(b) which shows that
 corrected synthetic seismograms are in good agreement with the experimental ones with a
 correlation coefficient greater than 0.92 in each case. These values of correlation coefficient
 are not as good as the previous ones. This can be explain, first by the fact that the 3D-
 2D geometrical spreading correction applied to experimental traces is not fully efficient for
 425 later arrivals, and second we have neglected effects of quality factors. Consequently, the
 estimated source is close to the real one but contains the inaccuracies from both numerical
 modeling and geometrical spreading correction.

However, these last results, based on an average estimated source wavelet show that the

effective impulse source emitted by the transducer in the MUSC laboratory measurement

430 bench is stable enough to ensure a robust reproducibility of the source for a complete physical experiment with multiple source and receiver positions. Therefore, concerning the key issue of the source knowledge, experimental data acquired in the MUSC laboratory can be efficiently processed by imaging methods like Full Waveform Inversion (FWI) with only one estimation step for all the multi-source and multi-receivers data.

435 In the previous approaches developed for the geometrical spreading correction calibration and the source estimation, the studies have been conducted on an homogeneous block of F50 epoxy-resin. This approach facilitates developments and applications but limits the validation to a simple media with simple acquisition geometry. Thus, we consider here a more complex model, called *BiAlt* (figure 3). The acquisition setup is composed

440 of shots with 241 receivers spaced of $\Delta r = 0.5 \text{ mm}$. The receiver line of 120 mm long is centered on the medium axis, where the topography of the 2-layer interface lays out a valley-shape curve 25 source positions are considered, ranging from 0 to 241 mm with a spacing $\Delta s = 1 \text{ mm}$. The source wavelets are modeled by a Ricker function with a central frequency equal to $f_0 = 75 \text{ kHz}$ and the parameter $t_0 = 0.03 \text{ ms}$. A low-pass Butterworth

445 filter ($\omega_c = 200 \text{ kHz}$) and a cosine taper are applied to the data. Given that the top layer of the model is made of the same epoxy-resin like for the homogeneous block, we applied the hybrid geometrical spreading correction with the same parameters. Corresponding synthetic data were generated using a 2-D SEM algorithm. Again, the quality factor is not taken into account. Figure 11(a) shows the efficient source wavelet estimated from the 241×25 traces

450 compared to the theoretical one. In this case, the estimated source wavelet seems more *i.e.* more symmetric than those recovered for the previous experiment. Moreover, few and very low amplitude multiple echoes occur compared to the previous estimated wavelet. This can

be related to the lower central frequency of the source which may generate less multiple at the interface between piezoelectric source. Again, this estimated source is applied to the synthetic data and the resulting traces for the first source are shown in figure 11(b). The comparison between the experimental traces (black) and numerical traces computed with the theoretical source wavelet (red) shows that the relative amplitude between P and S wavefront are very different, in particular between intermediate and far offset, which can be, again, related to a low quality factor for S-wave of the *LAB1000* epoxy-resin. Also, a phase shift appears progressively and is clearly visible at far offset, denoting inaccuracy in the P- and S- wave velocity estimation of the epoxy-resins. However, there is still a good agreement between experimental traces and numerical ones. Given that the effective source is estimated using a realistic multisource-multireceiver acquisition design over 25 source positions, this results confirms the stability of the source during large experimental campaigns.

CONCLUSIONS

High-resolution seismic imaging methods are mostly developed in the 2-D approximation and need real data to complete the validation of the inversion process often limited to inverse crime. We have demonstrated here that geometrical spreading and amplitude corrections usually used to transform 3-D in 2-D real seismic data is limited and can be replaced by accurate experimental 2-D data recorded in controlled environment. This alternative process has been shown to be more accurate when taking into account all the arrival, specially when reflected echoes interfere to the direct arrivals.

In a second step, the effective source wavelet emitted in the material after the coupling effect of the transducer as well as its possible variability have been studied. Given that the

475 knowledge of the source is an important task for some seismic data inversion algorithm.

Source estimation is widely done using the linear source wavelet estimation method which integrate the entire signal and is strongly dependent of the numerical initial model accuracy. Then, it is preferable to have the same source wavelet during a complete experiment. In this scope, we have studied the experimental source and validate its high reproducibility
480 for multisource-multireceiver experiments in case of an homogeneous medium but also for a two-layer model with a variation of the topography of the internal interface. the great repeatability of the recovered source wavelet as well as the high correlation coefficient of the simulated data in comparison to the experimental ones show the quality of the experimental data carried out through the reduced scale measurement bench MUSC.

485 Thus these studies have allowed to refine the capacity of the physical modeling designed for seismic experiments simulation.

Further studies will deal to the Quality factor estimation in order to avoid the normalization step in the process and to provide several sets of experimental data to the scientific community that will be perfectly controlled.

ACKNOWLEDGMENTS

490 CEA for the SEM3D Spectral Element Method modeling code. Access to the high-performance computing facilities of CCIPL (Nantes, France) provided the required computer resources and we gratefully acknowledge this facility and the support of the staff. Finally, this study was carried out within the framework of the VIBRIS project (OSUNA-IFSTTAR-CNRS) sponsored by Région Pays-de-la-Loire (France).

PLOTS

495 Figures

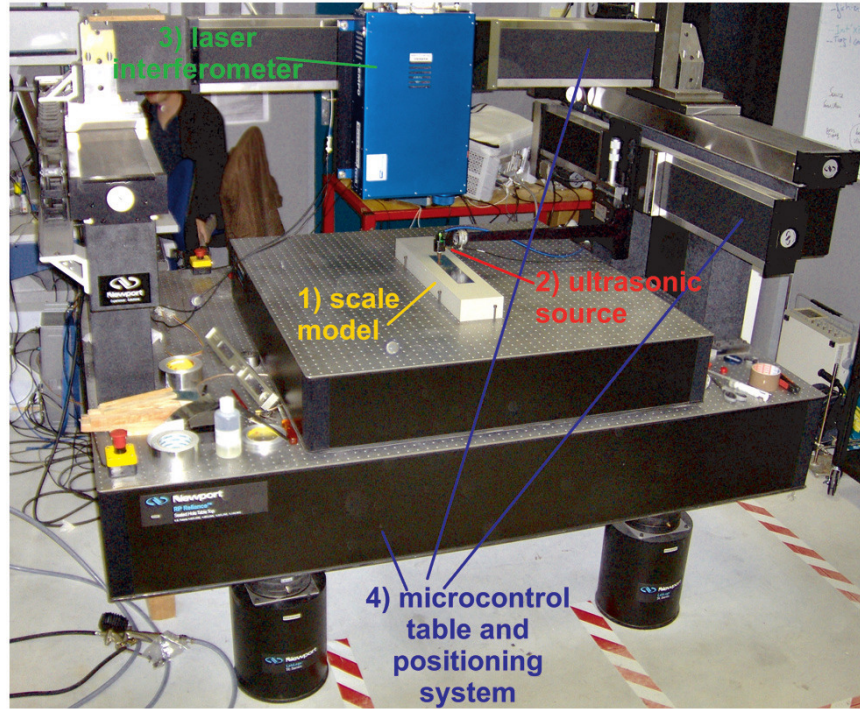


Figure 1: Photograph of the MUSC ultrasonic laboratory (from Bretaudeau et al. (2013)) with its four components: (1) a small-scale model of the underground, (2) an optical table with two automated arms moving above the model, (3) a laser interferometer recording ultrasonic wave propagation at the model surface, (4) a piezoelectric ultrasonic source generating ultrasonic waves in the model.

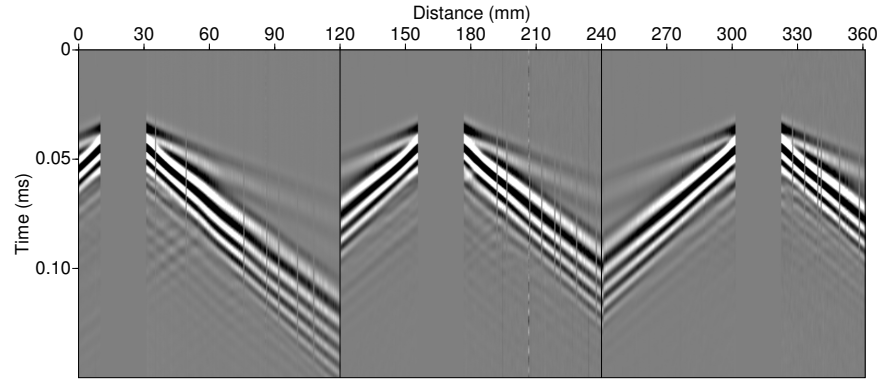


Figure 2: Example of multi-source multi-receiver record on the MUSC laboratory for a two-layer model (*BiAlt*).

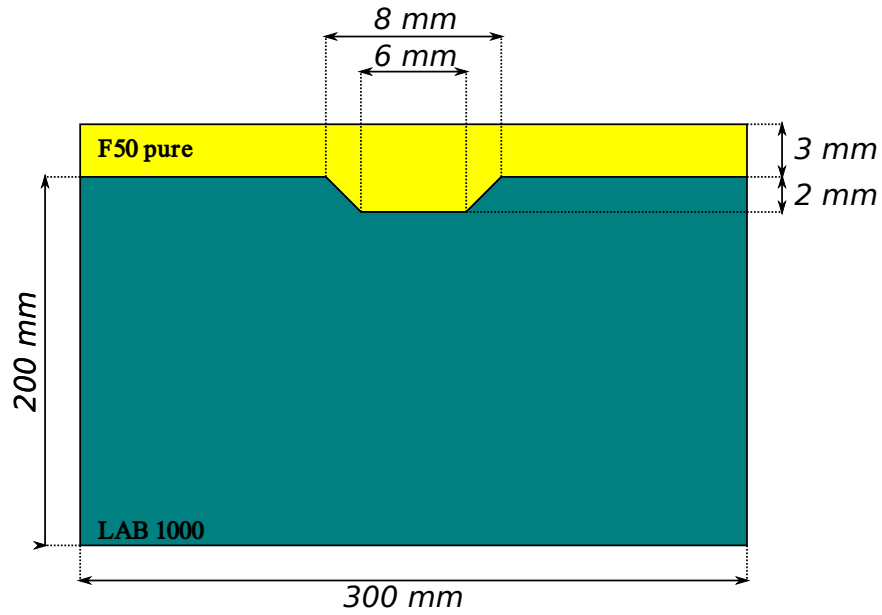


Figure 3: Schematic representation of the so-called *BiAlt* model.

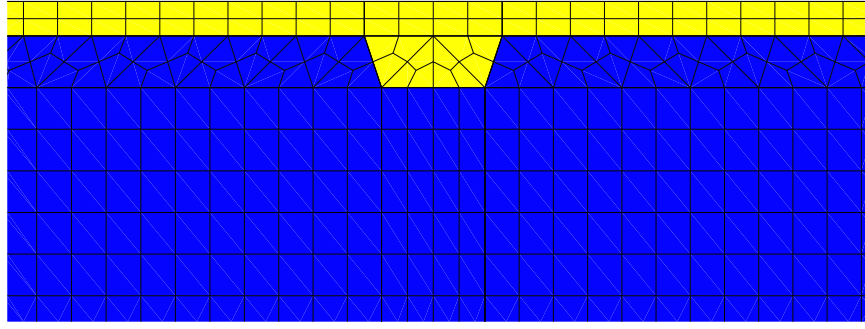


Figure 4: Zoom in the mesh of the *BiAlt* model used for numerical modeling.

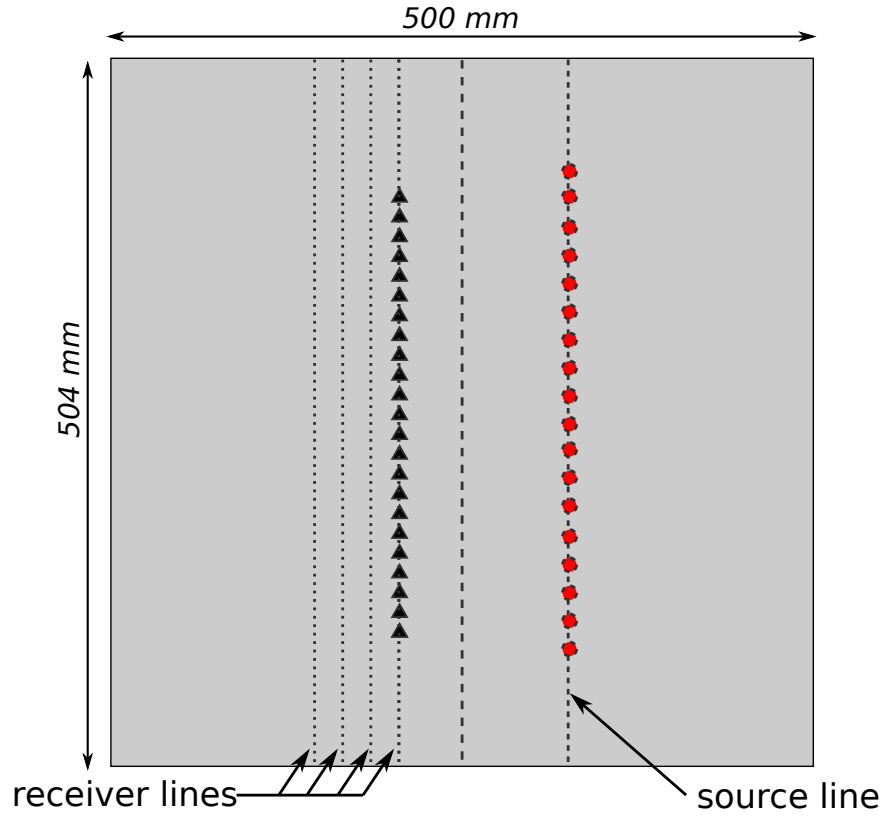


Figure 5: Schematic representation of the acquisition geometry used to generate experimental line-source, *i.e.* an equivalent of cylindrical source use in two-dimensional modeling. Black triangle and red circle represent receivers and sources, respectively.

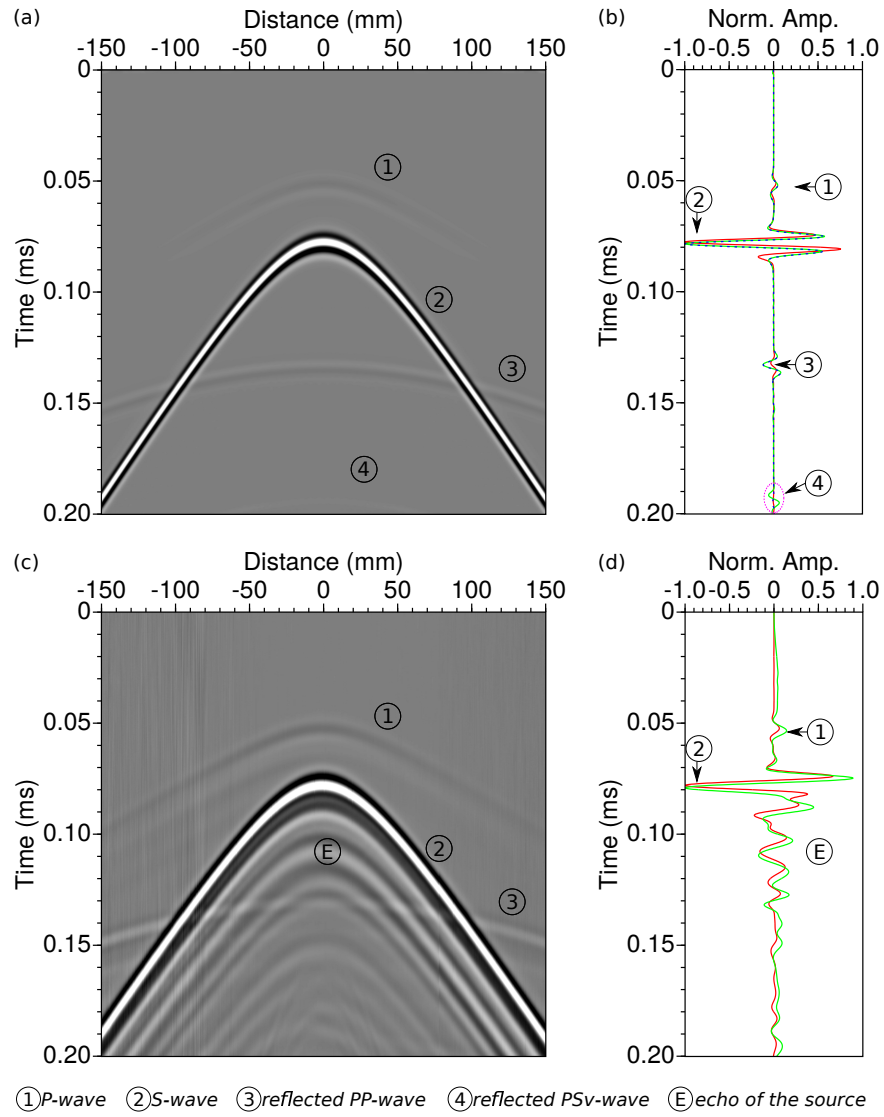


Figure 6: (a,b) Numerical modeling. (a) Resulting seismogram at one receiver position for the experimental line-source. (b) Comparison between point-source response in red (central trace of (a)), weighted stack response of (a) in green and line-source response from 2-D modeling in blue. (c,d) Same as (a) and (b) but for experimental modeling.

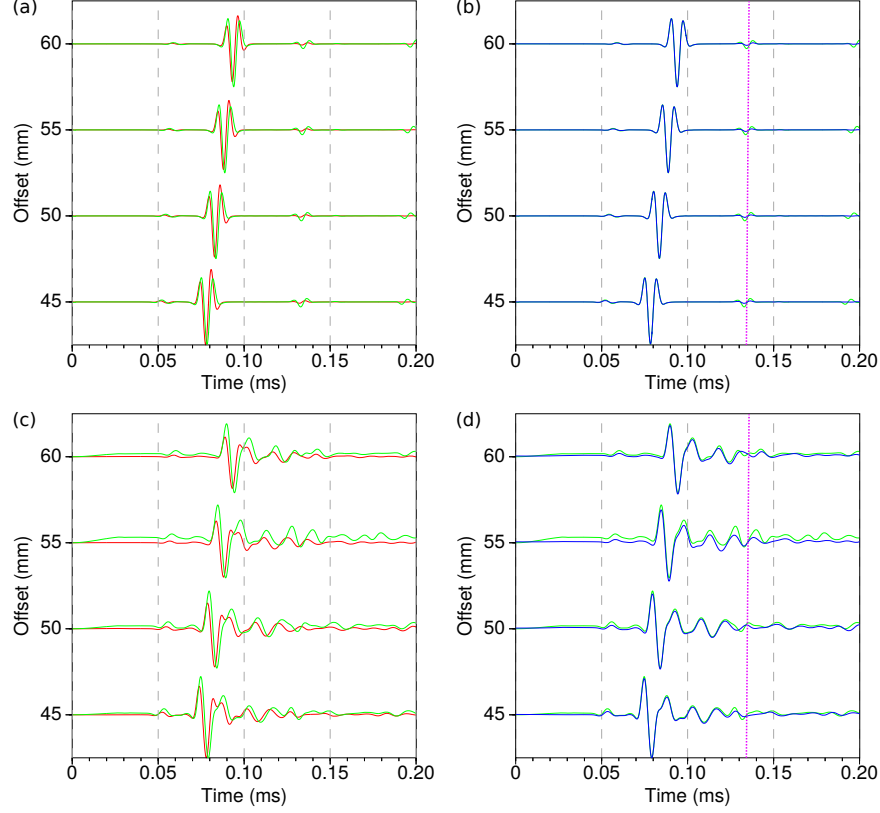


Figure 7: (a,b) Numerical modeling. (a) Comparison between synthetic seismograms for a point-source (red) and for a line source (green), for 45, 50, 55 and 60 mm source-receiver offsets respectively. (b) Comparison between synthetic seismograms for a line-source (green), and a point-source response corrected from geometrical spreading (blue) for same source-receiver offsets as (a) using the hybrid method with ratios $r = 0.35$, $r = 0.40$, $r = 0.45$ and $r = 0.50$ for offsets 45, 50, 55 and 60 mm, respectively. (c,d) Same as (a) and (b) for experimental modeling. The light-purple dotted lines pick PSv -wavefront.

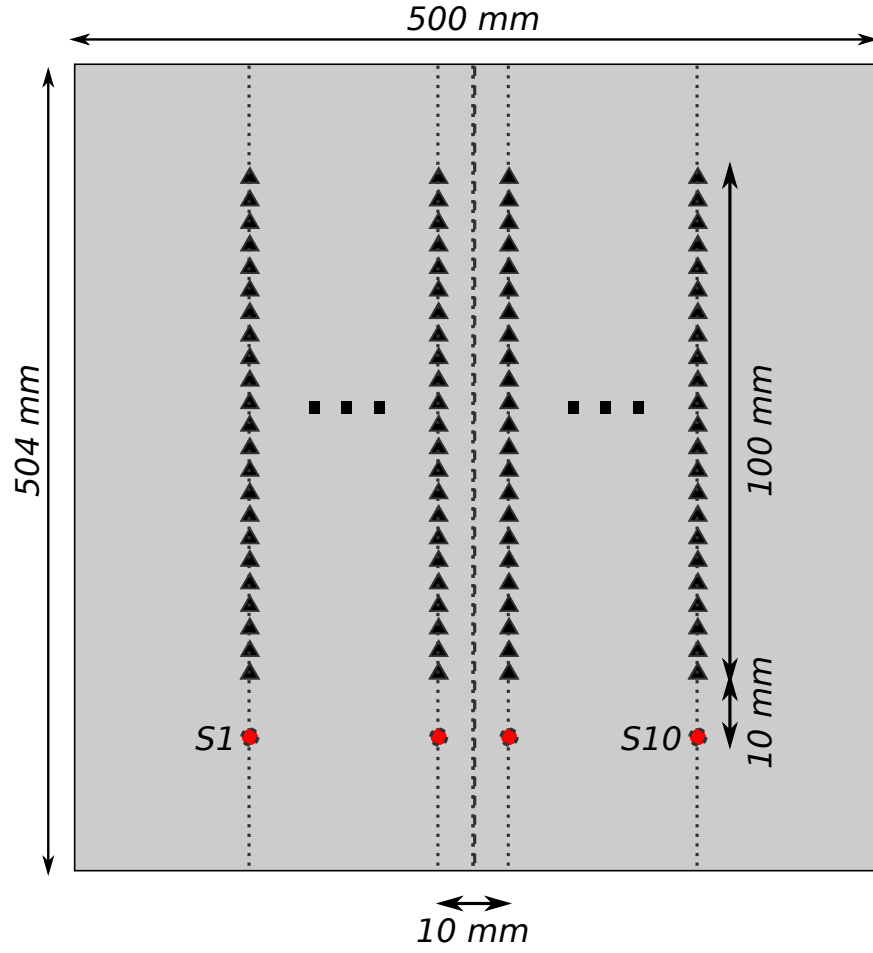


Figure 8: Schematic representation of the acquisition geometry used to assess the data reproducibility using the MUSC laboratory. Black triangle and red circle represent receivers and sources, respectively.

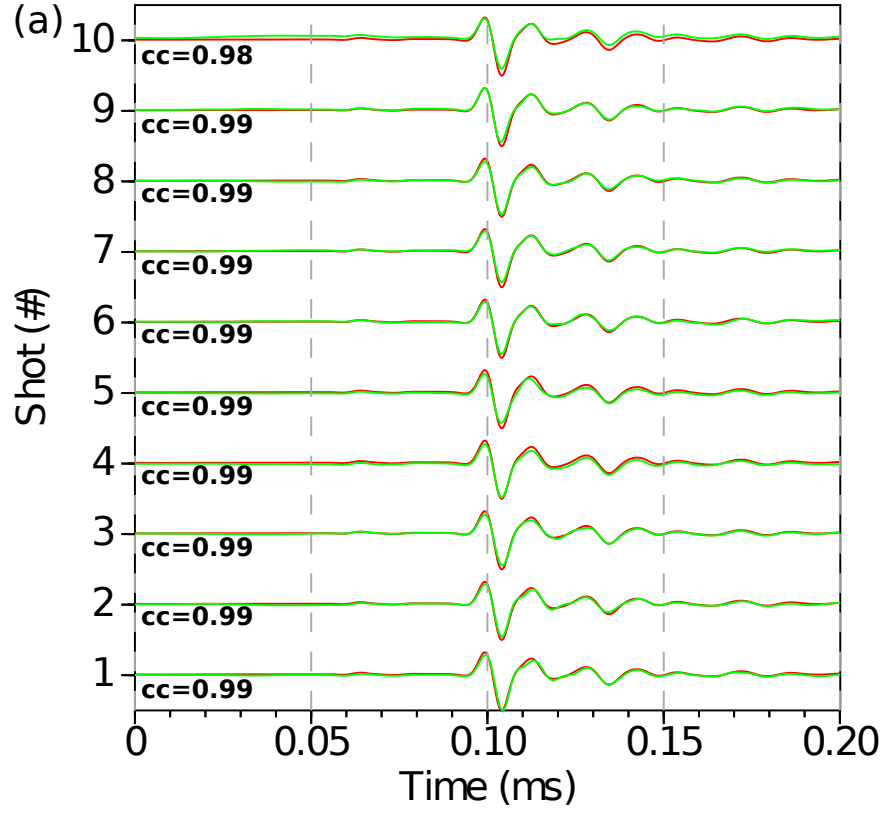


Figure 9: Central trace for each of the ten analogical experiment compared to a mean central trace (green). **cc** gives the correlation coefficient between the compared traces.

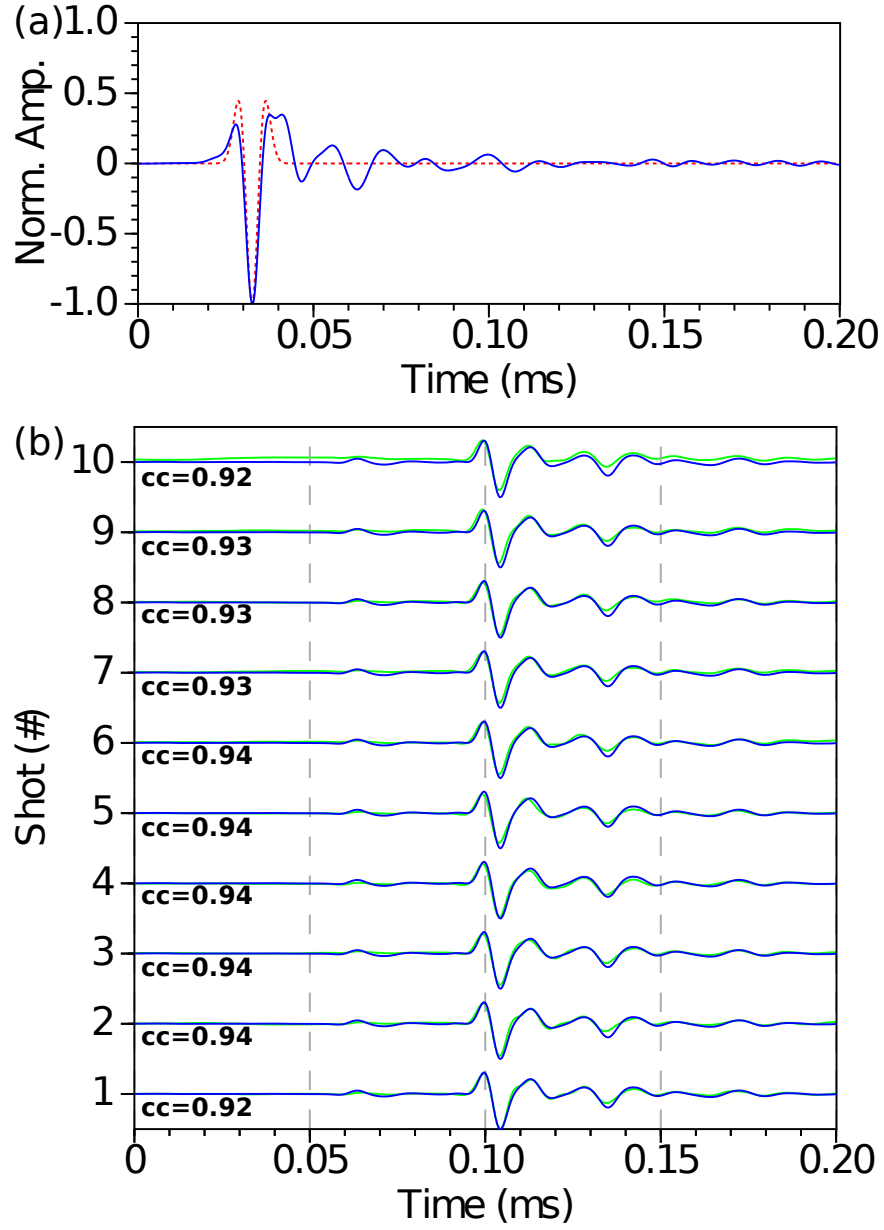


Figure 10: (a) Comparison between theoretical Ricker source ($f_0 = 100 \text{ kHz}$, $t_0 = 0.03 \text{ ms}$) send to the piezoelectric transducer (dashed red line) and the effective source for the homogeneous *F50 pure* model (blue line). (b) Comparison between experimental central traces and numerical ones using the effective source instead theoretical one. **cc** gives the correlation coefficient between experimental and synthetic traces.

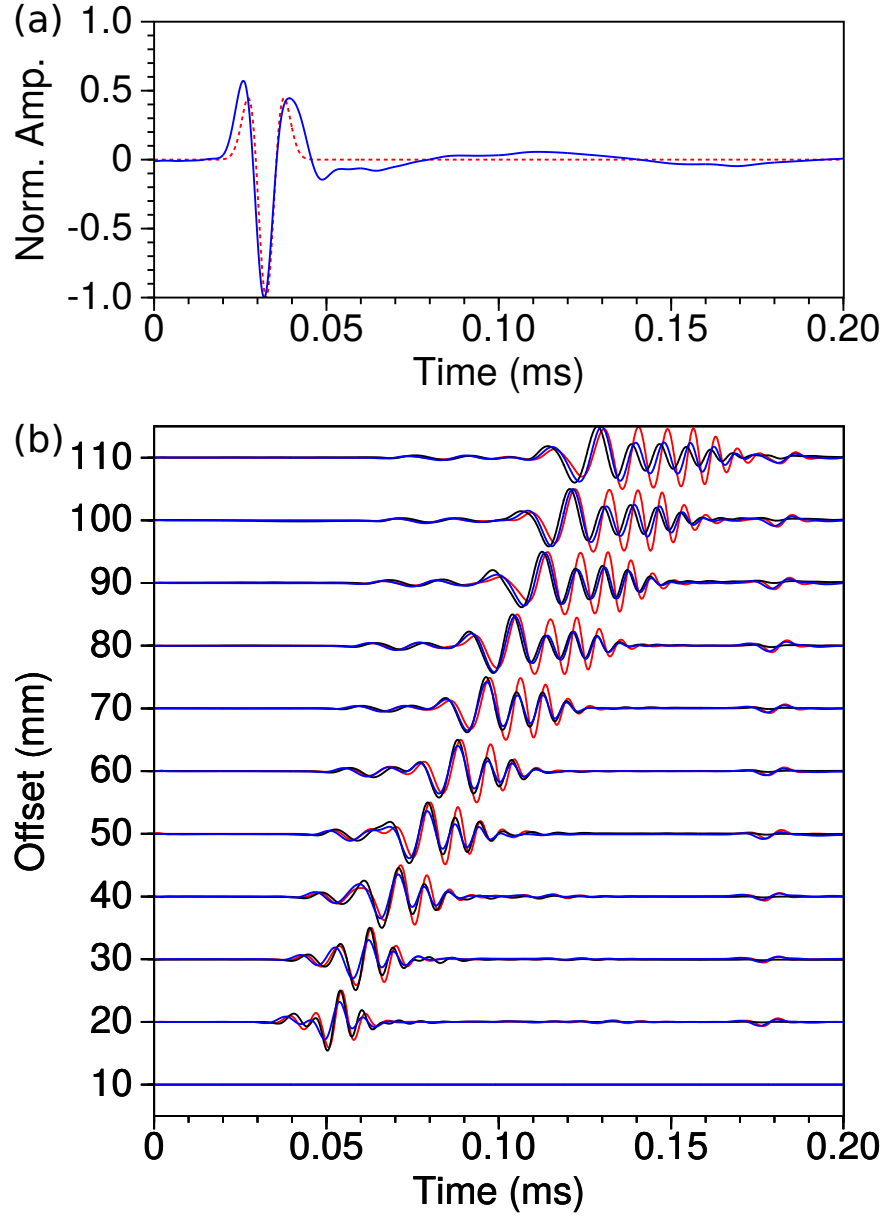


Figure 11: (a) Comparison between theoretical Ricker source ($f_0 = 75 \text{ kHz}$, $t_0 = 0.03 \text{ ms}$) send to the piezoelectric transducer (dashed red line) and the effective source for the *BiAlt* model (blue line). (b) Comparison between experimental central traces (black), numerical traces using theoretical source (red) and numerical traces using the effective source (blue).

Tables

| material | Field experiment scale | MUSC experiment scale | scales ratio |
|------------------|------------------------|-----------------------|--------------|
| P waves velocity | V_{p0} | V_{p0} | 1 |
| S waves velocity | V_{s0} | V_{s0} | 1 |
| Time | T_0 | $0.001 T_0$ | 0.001 |
| frequency | F_0 | $1000 F_0$ | 1000 |
| Distance | D_0 | $0.001 D_0$ | 0.001 |
| Wavelength | D_0 | $0.001 D_0$ | 0.001 |

Table 1: example of possible scales ratio between field experiments and MUSC experiments when considering a ratio equal to 1 for the density and Quality factor.

| material | Field experiment scale | MUSC experiment scale | scales ratio |
|------------------|------------------------|-----------------------|--------------|
| P waves velocity | V_{p0} | $2V_{p0}$ | 2 |
| S waves velocity | V_{s0} | $2V_{s0}$ | 2 |
| Time | T_0 | $0.001 T_0$ | 0.001 |
| frequency | F_0 | $2000 F_0$ | 2000 |
| Distance | D_0 | $0.001 D_0$ | 0.001 |
| Wavelength | D_0 | $0.001 D_0$ | 0.001 |

Table 2: example of possible scales ratio between field experiments and MUSC experiments when considering a ratio equal to 2 for the density and Quality factor.

| material | V_P (m/s) | V_S (m/s) | V_R (m/s) | ρ (kg/m ³) | Q |
|----------|-------------|-------------|-------------|-----------------------------|----|
| Aluminum | 5630 | 3225 | – | 2700 | – |
| F50 pure | 2300 | 1030 | 965 | 1300 | 30 |
| F50 200% | 2820 | 1425 | 1328 | 1766 | – |
| F50 240% | 2968 | 1496 | 1388 | 1822 | – |
| LAB1000 | 2850 | 1400 | 1310 | 1500 | 75 |

Table 3: Physical properties of some materials used to build small scale models. V_P , V_S and V_R are the P-wave velocity, S-wave and the Rayleigh wave velocity, respectively. ρ is the density and Q is the quality factor.

REFERENCES

- Aki, K., and P. G. Richards, 2002, Quantitative seismology, **1**.
- Ben-Hadj-Ali, H., S. Operto, and J. Virieux, 2008, Velocity model building by 3d frequency-domain, full-waveform inversion of wide-aperture seismic data: Geophysics, **73**, VE101–
500 VE117.
- Berkhout, A., D. Verschuur, and G. Blacquiere, 2012, Illumination properties and imaging promises of blended, multiple-scattering seismic data: a tutorial: Geophysical Prospecting, **60**, 713–732.
- Bohm, G., J. M. Carcione, D. Gei, S. Picotti, and A. Michelini, 2015, Cross-well seismic
505 and electromagnetic tomography for co 2 detection and monitoring in a saline aquifer: Journal of Petroleum Science and Engineering, **133**, 245–257.
- Borisov, D., and S. C. Singh, 2015, Three-dimensional elastic full waveform inversion in a marine environment using multicomponent ocean-bottom cables: a synthetic study: Geophysical Journal International, **201**, 1215–1234.
- 510 Bretaudeau, F., R. Brossier, D. Leparoux, O. Abraham, and J. Virieux, 2013, 2d elastic full-waveform imaging of the near-surface: application to synthetic and physical modelling data sets: Near Surface Geophysics.
- Bretaudeau, F., D. Leparoux, and O. Abraham, 2008, Small scale adaptation of the seismic full waveform inversion method - application to civil engineering applications.: The
515 Journal of the Acoustical Society of America, **123**.
- Bretaudeau, F., D. Leparoux, O. Durand, and O. Abraham, 2011, Small-scale modeling of onshore seismic experiment: A tool to validate numerical modeling and seismic imaging methods: Geophysics, **76(5)**, T101–T112.
- Castellanos, C., V. Etienne, G. Hu, S. Operto, R. Brossier, J. Virieux, et al., 2011, Algo-

520 rithmic and methodological developments towards full waveform inversion in 3d elastic
media: Presented at the 2011 SEG Annual Meeting, Society of Exploration Geophysicists.

Cristini, P., and D. Komatitsch, 2012, Some illustrative examples of the use of the spectral-
element method in ocean acoustics.: *Journal of the Acoustical Society of America*.

Dhatt, G., and G. Touzot, 1984, *The finite element method, displayed.*: John Wiley & Sons.

525 Favretto-Cristini, N., A. Tantsereva, P. Cristini, B. Ursin, D. Komatitsch, and A. Aizen-
berg, 2013, Numerical modeling of zero-offset laboratory data in a strong topographic
environment: results for a spectral-element method and a discretized kirchhoff integral
method: *Earthquake Science*.

Festa, G., and J. Vilotte, 2005, The Newmark as velocity-stress time-staggering: an efficient
530 PML implementation for spectral element ssimulation of elastodynamics: *Geophysical
Journal International*, **161**, 798–812.

Forbriger, T., L. Gross, and M. Schafer, 2014, Line-source simulation for shallow-seismic
data. part 1: theoretical background: *Geophysical Journal International*, **198**, 1387–1404.

Geuzaine, C., and J. Remacle, 2009, Gmsh: a three-dimensional finite element mesh gener-
535 ator with built-in pre- and post-processing facilities.: *International Journal for Numerical
Methods in Engineering*, **79**, 1309–1331.

Guofeng, L., L. Yaning, R. Li, and M. Xiaohong, 2013, 3d seismic reverse time migration
on gpgpu: *Computers & Geosciences*, **59**, 10–23.

Hulbert, G. M., and T. J. Hughes, 1990, Space-time finite element methods for second-
540 order hyperbolic equations: *Computer Methods in Applied Mechanics and Engineering*,
84, 327–348.

Komatitsch, D., R. Martin, J. TROMP, M. A. TAYLOR, and B. A. WINGATE, 2001,
Wave propagation in 2-d elastic media using a spectral element method with triangles

- and quadrangles: *Journal of Computational Acoustics*, **9**, 703–718.
- 545 Komatitsch, D., and J. Tromp, 1999, Introduction to the spectral-element method for three-dimensional seismic wave propagation: *Geophysical Journal International*, **139**, 806–822.
- Komatitsch, D., S. Tsuboi, and J. Tromp, 2005, The spectral-element method in seismology.
- Komatitsch, D., and J.-P. Vilotte, 1998, The spectral element method: an efficient tool to simulate the seismic response of 2d and 3d geological structures: *Bulletin of the seismological society of America*, **88**, 368–392.
- 550 Komatitsch, D., J. P. Vilotte, R. Vai, J. M. Castillo-Covarrubias, and F. J. Sánchez-Sesma, 1998, The Spectral Element Method for Elastic Wave Equation: Application to 2-D and 3-D Seismic Problems: *International Journal for Numerical Methods in Engineering*, **45**, 1139–1164.
- 555 ———, 1999, The spectral element method for elastic wave equations-application to 2-d and 3-d seismic problems: *International Journal for numerical methods in engineering*, **45**, 1139–1164.
- Lysmer, J., and L. A. Drake, 1972, A finite element method for seismology: *Methods in computational physics*, **11**, 181–216.
- 560 Martin, G. S., R. Wiley, and K. J. Marfurt, 2006, Marmousi2: An elastic upgrade for marmousi: *The Leading Edge*, **25**, 156–166.
- Moczo, P., J. Kristek, M. Galis, E. Chaljub, and V. Etienne, 2011, 3-d finite-difference, fine-element, discontinuous galerkin and spectral-element schemes for their accuracy with respect to p-wave to s-wave speed ratio: *Geophysical Journal International*.
- 565 Morozov, I., 2004, Crustal scattering and some artefacts in receiver function images: *Bulletin of the Seismological Society of America*, **94**, 1492–1499.
- Perez Solano, C., D. Donno, and H. Chauris, 2014, Alternative waveform inversion for

- surface wave analysis in 2-d media: *Geophysical Journal International*, **198**, 1359–1372.
- Plessix, R.-E., G. Baeten, J. W. de Maag, M. Klaassen, Z. Rujie, T. Zhifei, et al., 2010,
 570 Application of acoustic full waveform inversion to a low-frequency large-offset land data
 set: Presented at the 2010 SEG Annual Meeting, Society of Exploration Geophysicists.
- Pratt, R. G., 1999, Seismic waveform inversion in the frequency domain, Part 1: Theory
 and verification in a physical scale model: *Geophysics*, **64**, 888–901.
- Schafer, M., L. Gross, T. Forbriger, and T. Bohlen, 2014, Line-source simulation for shallow-
 575 seismic data. part2: full-waveform inversion – a synthetic 2-d case study: *Geophysical
 Journal International*, **198**, 1405–1418.
- Seron, F. J., F. J. Sanz, M. Kindelan, and J. I. Badal, 1990, Finite-element method for
 elastic wave propagation: *Communications in applied numerical methods*, **6**, 359–368.
- Tromp, J., D. Komatitsch, and Q. Liu, 2008, Spectral-element and adjoint methods in
 580 seismology.: *Commun Comput Phys*.
- Virieux, J., and S. Operto, 2009, An overview of full-waveform inversion in exploration
 geophysics: *Geophysics*, **74**, WCC1WCC26.
- Wirgin, A., 2004, The inverse crime: *ArXiv Mathematical Physics e-prints*. (Provided by
 the SAO/NASA Astrophysics Data System).
- 585 Wong, J., K. W. Hall, E. V. Gallant, R. Maier, M. Bertram, and D. C. Lawton, 2009,
 Seismic physical modeling at university of calgary: *CSEG recorder*, **34**.